Check for updates

Data-driven models for predictions of geometric characteristics of bead fabricated by selective laser melting

Thai Le-Hong[1,2] · Pai Chen Lin[3,4] · Jian-Zhong Chen[3,4] · Thinh Duc Quy Pham[1,5] · Xuan Van Tran[1]

Abstract

In this paper, the effects of two key process parameters of the selective laser melting process, namely laser power and scanning speed, on the single-track morphologies and the bead characteristics, especially the depth-to-width D/W and height-to-width H/W ratios, were investigated using both experimental and Machine Learning (ML) approaches. A total of 840 single tracks were fabricated with several combinations of laser power and scanning speed levels. Surface morphologies of the single tracks and bead profiles were thoroughly investigated, providing a track-type map and the evolutions of the bead characteristics as a function of laser power and scanning speed. The results indicate neither severe balling nor keyholing effect for all combinations of laser power and scanning speed. Besides, simple relationships cannot accurately describe the evolutions of the D/W and H/W ratios as a function of laser power and scanning speed. Two Machine Learning-based regression models, Random Forest and Artificial Neural Network, were chosen to estimate the D/W and H/W ratios using laser power and scanning speed. The Bayesian optimization algorithm was employed to optimize the model hyperparameter selection. Both Machine Learning-based models appear to be able to predict reasonably well the two aspect ratios, D/W and H/W, with an overall R^2 value reaching about 90%, evaluated on the cross-validation dataset after a few seconds of training time, respectively.

Keywords Selective melting laser · Bead geometry · Single-track morphology · Machine learning · Artificial neural network · Bayesian optimization

Introduction

Known as one of the most attractive metal-based Additive Manufacturing (AM) processes, selective laser melting (SLM) exhibits several advantages over the traditional manufacturing methods, such as its ability to produce high-quality parts in a single step and a reduced lead time with almost no limitation in shape and geometry (Santos et al., 2006). In addition, the items fabricated by this method can achieve a very high dimensional accuracy and good surface roughness (Zhang et al., 2018), reducing the number of post-processing required. This allows the SLM process to become tremendously attractive in the industry, especially for biomedical applications (Trevisan et al., 2018), automotive (Leal et al., 2017) and aerospace industries (Mohd Yusuf et al., 2019).

Technically, the SLM technology uses a laser as the heat source to radiate and fully melt successive layers of powder particles predeposited on a substrate, forming a component whose shape and structure are predefined in a three-dimensional computer-aided design model. As a powder-based AM method, the SLM process may involve several complex physical phenomena, such as interaction laser-metallic particles (laser absorption and reflection); fluid flow and Marangoni convection in the melt pool; heat transfer by conduction, convection, and radiation; rapid particle melting and solidification; heat accumulation and re-heating of the printed layers leading to re-melting and re-solidification; molten metal flow due to surface tension gradient affected

✉ Xuan Van Tran
  xuantv@tdmu.edu.vn

[1] Institute of Development Strategies, Thu Dau Mot University, Thu Dau Mot, Binh Duong 75100, Vietnam

[2] IMSIA, CNRS, EDF, CEA, ENSTA Paris, Institut Polytechnique de Paris, 828 Boulevard des Maréchaux, 91762 Palaiseau, France

[3] Advanced Institute of Manufacturing with High-Tech Innovations, National Chung-Cheng University, Chia-Yi 62102, Taiwan

[4] Department of Mechanical Engineering, National Chung-Cheng University, Chia-Yi 62102, Taiwan

[5] Mécanique des Solides et des Matériaux, Université de Liège, Liège, Belgium

by temperature variation; evaporation and mass transfer of materials; recoil pressure due to metal evaporation (Papazoglou et al., 2020). These phenomena are considered as determining factors for the creation of the melt pool that, in its turn, has a strong impact on the formation of defects (porosity, surface roughness, residual stresses, distortion, and cracking initiation) and the phase transformation (Guo et al., 2019)—which determine the qualities of the final products. As a result, to better understand the SLM mechanisms and fabricate components with higher quality and fewer manufacturing defects, it is vital to comprehend and control the melt pool geometrical characteristics as well as its affecting parameters.

For that purpose, the geometries of the single-track and multi-track melt pool created during the SLM process have been extensively investigated to identify the effects of SLM processing parameters on defect formation mechanisms, especially porosity and surface roughness (Ahsan & Ladani, 2020; Di et al., 2012; Dilip et al., 2017; Gu et al., 2020; Guo et al., 2019; Kusuma et al., 2017). Among them, laser power and scanning speed have been found to affect single-track beads the most and directly through the energy input (Di et al., 2012; Greco et al., 2020; Kamath, 2016). Indeed, under high energy input intensity, characterized by high laser power and low scanning speed, the temperature absorbed by the material particles can locally exceed the vaporization temperature of some elements (Ahsan & Ladani, 2020), leading to the formation of cavities named keyhole within the melt pool or on the surface of the final part. This can be considered as a result of a high recoil pressure, which is higher than the surface tension and hydrostatic pressure of the metal liquid (Papazoglou et al., 2020). In this scenario, the melt pool creation is principally dominated by recoil pressure and fluid dynamics (Qi et al., 2017; Yang et al., 2016). Besides, a large penetration depth of the melt pool and a small heat-affected zone (HAZ) can be observed, resulting in a very high depth-to-width ratio. In contrast, at low or moderate energy intensity, the heat transfer through conduction plays a dominant role in the melt pool creation (Le & Lo, 2019), which may help form a better bead morphology of the single tracks (Papazoglou et al., 2020).

It was shown that a lower energy density, resulting from a diminished laser power and/or an increased scanning speed, can decrease the bead depth considerably by reducing the transmission of energy absorbed, leading to a decrease in the depth-to-width ratio (Guo et al., 2019; He et al., 2019). By simulation, Papazoglou et al. indicated that a small depth-to-width ratio lower than 0.5 might be considered as an indicator of conduction mode (Papazoglou et al., 2020). This is consistent with experimental observations in He et al., (2019), King et al., (2014). Additionally, Dilip et al. showed that a depth-to-width ratio of around 0.37–0.6 is necessary to achieve good welding of the printed track with the substrate (Dilip

et al., 2017). Besides, an insufficient energy input can lead to a very high height-to-width bead ratio by slightly reducing the bead width and dramatically increasing the bead height (Guo et al., 2019). This phenomenon may be explained by the fact that, in this condition, the input energy is not sufficient so that the powders cannot be melted completely, or only a part of them in the center of the laser beam is melted. This tends to increase the metal liquid's viscosity within the molten pool as the laser power decreases and/or the scanning speed increases, reducing its wettability and spreading on the surface (Guo et al., 2019). Also, Tang et al. proposed a criterion for the lack of fusion on the basis of the total bead depth, including the cap height and the penetration depth (Tang et al., 2017). Indeed, to avoid the lack of fusion, the total depth of the bead needs to be larger than the layer thickness in the SLM process (Tang et al., 2017). In summary, it is essential to optimize the laser power and scanning speed to assure good bonding between layers of the printed parts as well as that with the substrate and avoid defect formation due to the keyholing effect or the lack of fusion.

It is important to note that most above-mentioned research conducted on the SLM bead geometry was based on thermohydraulic and finite element simulations (Ahsan & Ladani, 2020; Andreotta et al., 2017; Gao et al., 2020; Gu et al., 2020; Le & Lo, 2019; Le et al., 2020; Papazoglou et al., 2020), which have been considered less costly and time-consuming than experiments, leading to a limited number of experimental data available in each published research. However, due to the complexity of the physical phenomena likely encountered in an SLM process, as mentioned above, these models need many assumptions based on the heat source, laser absorption coefficient, effective thermal conductivity, heat losses, material properties, etc. (Papazoglou et al., 2020), which cannot be strictly justified in practice by experiments. For example, to simplify the problem, some studies were conducted by assuming a fixed laser absorption or temperature-independence for material properties and heat loss (convection and radiation), which are not correct in real life.

It should be noted that these researches mainly focused on the individual characteristics of the bead morphology, i.e., bead width, depth, height, and contact angle. The aspect ratios, i.e., depth-to-width and height-to-width, appear to be rarely mentioned in the literature for the SLM process. Characterizing the individual bead characteristics (height, depth, width) allows understanding of the effect of process parameters. However, the individual bead characteristics strongly depend on the experimental equipment, i.e., machine, laser type, laser spot size, etc., that potentially vary between laboratories. Therefore, in the literature, only the relative tendencies of the bead characteristics have been so far discussed, not their absolute values. The transferability of experimental results appears not to be possible from one laboratory to

another. In contrast, the aspect ratios can be considered as normalized bead characteristics, which allows an overview of the single-track bead resulting from multiple parameters. Indeed, in the literature, several studies have mentioned these ratios as indicators of delimiting the defects related to the melt pool creation, for example, lack of fusion or keyhole mode (Dilip et al., 2017; Guo et al., 2019; He et al., 2019; King et al., 2014; Papazoglou et al., 2020).

So far, several studies have attempted to propose simple relationships to correlate the bead characteristics, bead depth, height, and width, to laser power and scanning speed (Gao et al., 2020; Kusuma et al., 2017; Shi et al., 2017). All of them were purely based on fitting curves established from a small number of experimental data. From 25 experimental values, Kusuma et al. described the evolution of the bead width for commercially pure titanium as a linear function of the natural logarithm of the energy density, expressed by power-to-scanning speed ratio (P/v) (Kusuma et al., 2017). Gao et al. suggest a quadratic relationship of the track height and width with scanning speed on the basis of 5 simulations for 316L stainless steel, without mentioning laser power (Gao et al., 2020). From 36 single tracks fabricated on Ti-47Al-2Cr-2Nb, Shi et al. proposed that their geometric characteristics could be described by exponential models $y = kP^l v^m$, where k, l, and m are 3 model parameters to be adjusted (Shi et al., 2017). Except for the bead width for which the R^2 value can reach 0.94, those of the bead height and depth are relatively low, 0.40 and 0.61 (Shi et al., 2017). However, none of the two aspect ratios was studied using this approach up to now.

Machine Learning has been largely developed in the last years, especially in the AM field (Meng et al., 2020; Qi et al., 2019; Wang et al., 2020a, b). This method provides robust tools to deal with complex problems and data in a shorter time, reducing the demand for experimental and computational costs. However, most of the applications were limited to the printed components' ultimate properties, such as density ratio, surface roughness, tensile strength (Garg et al., 2018; Park et al., 2021; Wang et al., 2020a, b; Xia et al., 2021). Some studies used the ML methods for defect detection (Khanzadeh et al., 2018, 2019; Scime & Beuth, 2019). Others focused on developing models to predict temperature field (Mozaffar et al., 2018; Ren et al., 2020; Roy & Wodo, 2020) or thermal-induced stress/deformation (Mohajernia et al., 2019) during or after fabrication. A few studies on the prediction of bead geometry are available in the literature using the genetic algorithm for Wire Arc Additive Manufacturing (WAAM) (Panda et al., 2019) or using Artificial Neural Network (ANN) for robotic Gas Metal Arc Welding (GMAW)-based rapid manufacturing (Xiong et al., 2014). Tapia et al. employed the Gaussian process to develop a surrogate model to predict bead geometry fabricated by SLM for 316L stainless steel (Tapia et al., 2018). However, this study only focused on the depth penetration with a limited

number of experimental data, i.e., 97 data points collected from 3 different sources in the literature, knowing that the laser beam size used in these studies are different from one another besides other experimental conditions and equipment that potentially are not the same. Apart from this one, to the authors' best knowledge, none of the other Machine Learning-based studies have been performed on the geometrical characteristics of the bead made by the SLM process, especially the two aspect ratios, depth-to-width and height-to-width, for titanium-based alloy powders.
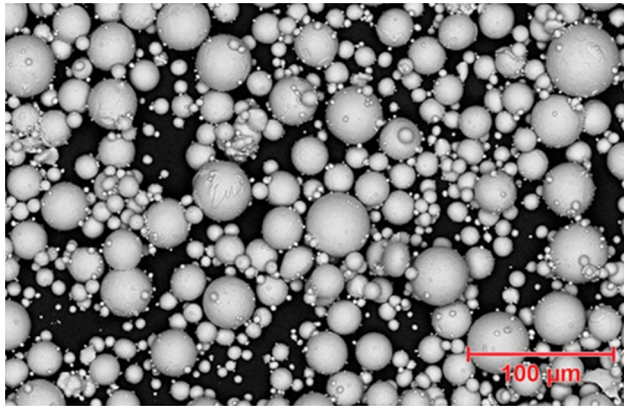
Our study is devoted to thoroughly investigating the influence of two key SLM processing parameters, including laser power and scanning speed, on the geometrical characteristics of the single tracks deposited by the SLM process for Ti–6Al–4V powder, which has attracted much interest for aerospace, biomedical, and defense applications (Dutta et al., 2017). Precisely, it aims to:

- provide a complete experimental database and an in-depth understanding of the bead characteristics' evolutions as a function of laser power and scanning speed, as well as the potentially complex relationship between them.
- identify the effects of process parameters on two aspect ratios, namely penetration depth-to-bead width D/W and bead height-to-width H/W, which have been rarely mentioned in previous studies.
- Build predictive models based on Machine Learning for these ratios using laser power and scanning speed. This can help optimize the process parameters to obtain high-quality single-track morphology with good inter-layers bonding as well as that between deposited layers and the substrate. It is worth noting that the main goal of this study is not to focus on Machine Learning development, but the application of Machine Learning in a new field to understand physical phenomena, more precisely in additive manufacturing.

The next section of this paper describes the materials and the experimental procedures used in this study. The Machine Learning methods and algorithms employed to build the predictive models as well as to optimize their hyperparameters are detailed in Sect. 3. The following section focuses on the experimental results and discussion on the effects of laser power and scanning speed on the track surface morphologies and the bead geometry. Also, in this section, the prediction of bead characteristics based on simple relationships is discussed. The paper ends with Sect. 4.3, in which the results obtained by Machine Learning methods, as well as the model performance and reliability, are presented and discussed in detail.

Table 1 Chemical composition of Ti–6Al–4V powder (in weight %)

Elements	Al	V	C	Fe	H	N	O	Ti
Ti–6Al–4V ELI Grade 23	6.2	4.0	0.10	0.14	0.003	0.02	0.07	Bal

Fig. 1 Scanning electron microscopy micrograph of Ti–6Al–4V powder

Table 2 Laser power and scanning speed values used to fabricate the single tracks by the SLM process

Process parameter	Unit	Level
Laser power (P)	W	200, 250, 300, 350, 400, 450, 500
Scanning speed (v)	mm/s	100, 200, 300, 400, 500, 600, 700, 800, 900, 1000, 1100, 1200, 1300, 1400, 1500, 1600, 1700, 1800, 1900, 2000

Materials and experimental procedures

Materials

The material used in this study is Ti–6Al–4V ELI Grade 23 powder supplied by LPW Technology Ltd, with the chemical composition listed in Table 1. The ELI stands for extra-low interstitial. As a result, the materials contain a relatively small amount of interstitial elements, *i.e.*, Fe, C, and O, in the chemical composition, which can help improve the strength and fracture toughness. The powder particle size varies from 20 to 63 μm, with a spherical shape, as shown in Fig. 1.

The samples were fabricated using an AMP-160 SLM machine supplied by TONGTAI Machine & Tool CO., LTD under the protection of argon (Ar) with the oxygen (O_2) content below 1000 parts per million (ppm), limiting the oxidation of the powder and printed samples at high temperature during the SLM process. The machine uses a fiber laser as the heat source with a nominal maximal power of 500 W, a 1070 ± 10 nm wavelength, and a laser spot size of 50 μm. The experiments were carried out at room temperature without preheating.

Experimental procedures

In order to investigate the effects of laser power and scanning speed, and generate the database for the predictive models, 10-mm-length single lines were deposited on the $100 \times 100 \times 3$ mm^3 substrates made of the same materials (Ti–6Al–4V) by considering 7 levels of laser power from 200 to 500 watts (W) with a 50 W increment coupled with 20 levels of scanning speed varying between 100 and 2000 mm/s,

as listed in Table 2. The laser power levels were chosen in such a way that they can be uniformly distributed between a low (200 W) and the maximal value of the machine used (500 W). Regarding the scanning speed, its values were uniformly selected between a very slow, 100 mm/s, and a very high speed, 2000 mm/s, based on our previous experience. The experiments were fabricated at a constant and sufficiently small layer thickness of 30 μm in the hope of avoiding the droplet formation by stabilizing the molten pool, which may lead to maximizing the relative density of bulk samples, as reported in Di et al., (2012), Greco et al., (2020), Park et al., (2021). The distance between the single lines was fixed to 1.05 mm to ensure no overlapping between successive lines. For each combination of laser power and scanning speed, 6 experiments were carried out to assure the reliability and reproducibility of the results. A total of 840 SLM single-tracks were fabricated in this study, as shown in Fig. 2.

Bead characteristic measurements

For the single track's geometrical characteristics, three features were investigated: bead height H, bead width W, and penetration depth D, as shown in Fig. 3. These characteristics were measured using a NIKON LV100ND optical microscope at the cross-section of the single tracks after sectioning, grinding, and polishing. The brighter-colored area under the bead (see Fig. 3) potentially corresponds to the heat-affected zone formed by heat transfer from the melt pool to the substrate during the AM process, commonly observed in welding and additive manufacturing processes (Kistler et al., 2019; Mahamood & Akinlabi, 2018). Two aspect ratios, depth-to-width (D/W) and height-to-width (H/W), were then calculated from the bead characteristics, namely bead height, width, and penetration depth. As discussed previously in Sect. 1, these two ratios can be used as indicators to determine the quality of a single track besides its surface morphology.

Fig. 2 Photograph of 10-mm-length single-tracks (thin horizontal lines) deposited by the SLM process on Ti-6Al-4 V plates
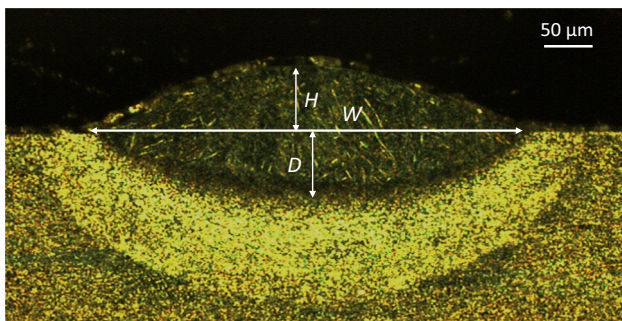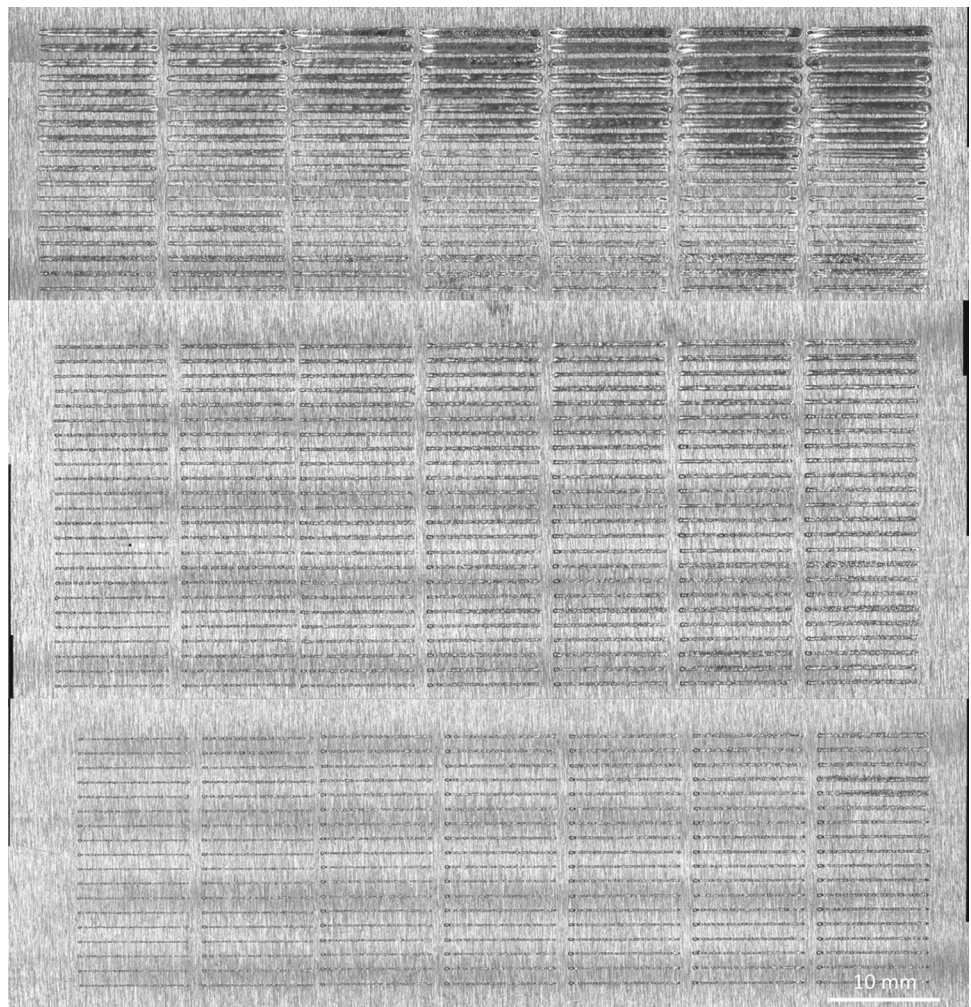

Fig. 3 Schematic of the geometrical characteristics (H: bead height, D: penetration depth, and W: bead width) of a single track at the cross-section

Machine learning models

Data preprocessing

This study aims to develop predictive models based on Machine Learning (ML) methods to estimate the two aspect ratios, depth-to-width (D/W) and height-to-width (H/W), using two process parameters considered as input variables, i.e., laser power (P) and scanning speed (v). For each couple of laser power and scanning speed, 6 experiments were conducted, and the reported values of D/W and H/W are those averaged. As a result, the dataset contains a total of 140 data points, corresponding to 140 averaged values, after performing 840 experiments, which were considered as output, as detailed hereafter. In this study, the inputs were composed of a vector of 140 rows containing 7 values of laser power and another one with 20 values of scanning speed, which have been shown in Table 2. The outputs consist of a matrix constituted of 2 column vectors of 140 rows corresponding to 2 aspect ratios, D/W and H/W. The dataset $\mathcal{D}$ used to train and validate the ML models can be represented as follows:

$$\mathcal{D} = \{(\boldsymbol{x}^{(i)}, \boldsymbol{y}^{(i)}), i = 1, ..., 140\} \tag{1}$$

where $\boldsymbol{x}$ is the input vector of P (laser power) and v (scanning speed). $\boldsymbol{y}$ is the vector of D/W and H/W. The raw dataset

used to train and validate the models can be found in the supplementary material of this paper.

To avoid the adverse effects potentially caused by the difference in the order of magnitude of the variables, hence speeding up the training convergence process and improving the model performance (Yun et al., 2018), both input and output variables were normalized in the range of 0 and 1 using the following equation:

$$x^{scaled} = \frac{x - x^{\min}}{x^{\max} - x^{\min}} \tag{2}$$

where x, $x^{\min}$, $x^{\max}$ correspond to the actual value of a variable and its maximum and minimum in the dataset, respectively. Then, the dataset was randomly split into training $\mathcal{D}_T$ and validation $\mathcal{D}_V$ datasets with a conventional ratio of 80 and 20%, respectively.

Machine learning regression models

Our framework consists of a supervised learning problem with multiple outputs. Precisely, the relationship between the input vector $\boldsymbol{x}$ and the output vector $\boldsymbol{y}$ is approximated by an ML-based regression model $\mathcal{F}$ from $\mathbb{R}^2 \to \mathbb{R}^2$ such that:

$$\boldsymbol{y} = \mathcal{F}(\boldsymbol{x}|\boldsymbol{\theta}), \tag{3}$$

where $\boldsymbol{\theta}$ is the learnable parameter of the ML algorithm (i.e., the weights and biases of the Artificial Neural Network-based model).

Among the ML-based regression algorithms, several models $\mathcal{F}$ representing different regression algorithm categories, from linear regression-based models, nonlinear regression-based models, to Boosting regression-based models, were tested. Two models were then selected: Random Forest (Aldous, 1993) and Artificial Neural Network (ANN) (Jain et al., 1996) due to their good accuracy for the prediction. Random Forest is an ML method widely used in data analysis for regression and classification due to its advantages, such as ease of use and interpretation, short training time, and relatively high accuracy (Unpingco, 2019). This technique is based on the learning (fitting) of multiple decision trees randomly built on sub-samples of the dataset, which are then averaged to progressively improve the model's predictive accuracy. Artificial Neural Network consists of several layers in which artificial neurons are interconnected, which is inspired by the human neural networks. This allows iteratively learning and solving complex problems using an error backpropagation algorithm (feedforward). The use of Artificial Neural Networks, as well as the involved parameters, were detailed in Park et al., (2021). The Random Forest and ANN models' hyperparameters were obtained using the Bayesian optimization algorithm (Snoek et al., 2012), as

detailed in Sect. 3.3 and Sect. 4.3.1. It is worth noting that this study focuses on the application of Machine Learning in an engineering field. Therefore, the detailed algorithms of these models, commonly used in Machine Learning, are not described in this paper.

The coefficient of determination R^2 metric was employed to assess the model performance. This metric measures the fitting capacity of the values predicted by the model and those of the observed data, based on a set of errors, which are the total sum of squares (SQ_{Total}) and the error sum of squares (SQ_{Error}), calculated between them as follows (Heumann et al., 2016):

$$R^2 = \frac{SQ_{regression}}{SQ_{Total}} = 1 - \frac{SQ_{Error}}{SQ_{Total}}, \tag{4}$$

$$SQ_{Total} = \sum_{i=1}^{n} (y_i - \overline{y})^2, \tag{5}$$

$$SQ_{Error} = \sum_{i=1}^{n} (y_i - \widehat{y_i})^2 \tag{6}$$

where y_i, $\widehat{y_i}$, and $\overline{y}$ are the actual value, the predicted value from the model, and the mean of the actual value, respectively. n represents the number of samples in the dataset. From its above-presented definition, an R^2 value closer to 1 signifies that the model is capable of producing a good fit for the observation data. However, it does not present the same conclusion for the model accuracy and goodness in terms of overfitting and/or underfitting that need to be assessed otherwise as detailed hereafter. Besides, it should be noted that the model is only trained on the training dataset to obtain the model weight and bias matrices, then the R^2 value is evaluated on a previously-unseen dataset by the model, i.e., the validation one.

Bayesian optimization for the Machine learning-based model hyperparameter selection

In the ML-based method, the model performance and its training convergence ability strongly depend on the selection of its hyperparameters, *i.e.*, the number of hidden layers in an ANN model. As a result, selecting a suitable set of hyperparameters is essential to obtain satisfactorily good results. For this purpose, several algorithms were developed and commonly used, such as Grid Search, Random Search, and the most recently developed one is the Bayesian optimization (BO)-based algorithm using the Gaussian process (Frazier, 2018). The irreplaceable advantage of the latter, compared to the two first methods, consists of its capacity to provide an automated hyperparameter optimization process, which is less time-consuming and more accurate. However, this method requires complex analytical capabilities, limiting its usage to real-life applications.

Fig. 4 Optical micrographs of the top surface of the SLM-built single tracks deposited with 500 W laser power and different scanning speed: **a** 100 mm/s, **b** 600 mm/s, **c** 1500 mm/s, and **d** 2000 mm/s
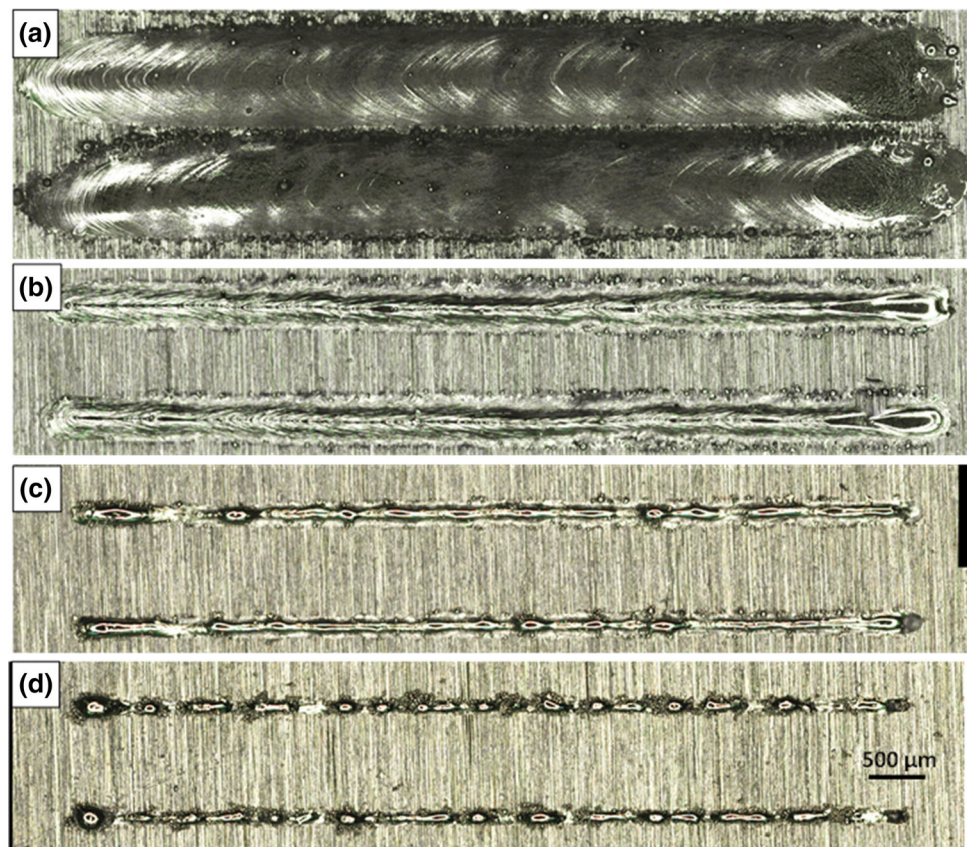
Following the recent development of a built-in Bayesian optimization library, i.e., Scitkit-Optimize library (Skopt) in Python, the aforementioned problem can be currently coped with straightforwardly. As a result, in this study, Bayesian optimization was chosen to optimize the selection of the ML-based model hyperparameters. The underlying theories (Bayes' Theorem and Gaussian process) and the application of the Bayesian optimization were detailed in Frazier (2018), Snoek et al., (2012), a brief introduction of this method can be presented as follows.
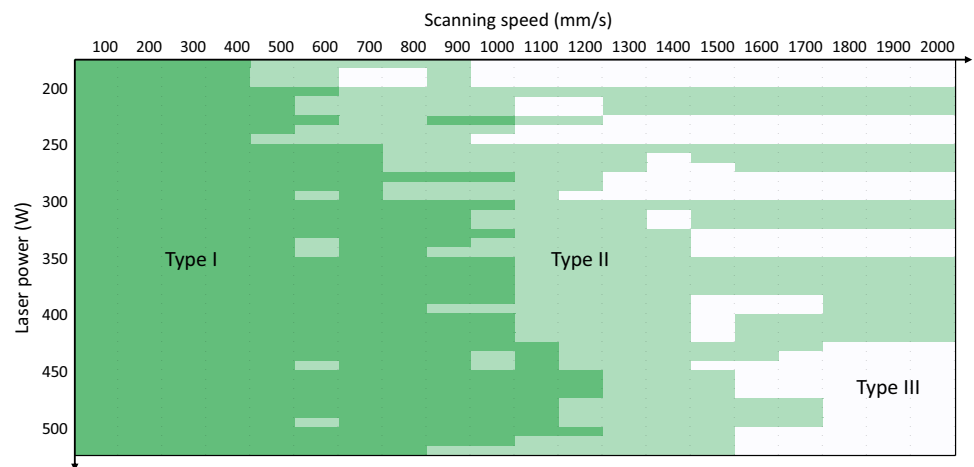
Let $\mathcal{D}_T^{t-1} = \{(\boldsymbol{\theta}^{(i)}, \boldsymbol{x}^{(i)}, \boldsymbol{y}^{(i)}), i = 1, ..., t-1\}$ be the training dataset consisting of the input–output pair $\boldsymbol{x}, \boldsymbol{y}$, and the hyperparameter $\boldsymbol{\theta} \in \mathcal{X}$ to be optimized such that $\boldsymbol{y} = \mathcal{F}(\boldsymbol{x}|\boldsymbol{\theta})$. The general procedure of BO to find the optimal hyperparameter $\boldsymbol{\theta}$ is summarized as follows:

Algorithm 1. Bayesian Optimization
• **Input:** hyperparameter space $\mathcal{X}$, data $\mathcal{D}_T^{t-1}$
For $t = 1, 2, ..., t_{\max}$
1. Find $\boldsymbol{\theta}^t$ by maximizing the acquisition function, $\mathcal{U}$ as: $$\boldsymbol{\theta}^t = arg \max_{\boldsymbol{\theta} \in \mathcal{X}} \mathcal{U}(\boldsymbol{\theta}|\,\mathcal{D}_T^{t-1}).$$
2. Sample the objective function $\boldsymbol{y}^t = \mathcal{F}(\boldsymbol{x}^t|\boldsymbol{\theta}^t)$
3. Augment the data $\mathcal{D}_T^t = \{\mathcal{D}_T^{t-1} \cup (\boldsymbol{\theta}^t, \boldsymbol{x}^t, \boldsymbol{y}^t)\}$ and update the posterior of $\mathcal{U}$
4. Repeat until $t = t_{\max}$
End
• **Output:** optimal $\boldsymbol{\theta}$

Fig. 5 Distribution of single-track types as a function of laser power and scanning speed for 840 experiments (type I: continuous and homogeneous track, type II: continuous and non-homogeneous track, type III: irregular track)

Fig. 6 Typical surface defects of SLM-built single tracks

In summary, the BO requires constructing an approximate surrogate model using the Gaussian process of the objective function $\mathcal{U}$, and then continuously updating the posterior of $\mathcal{U}$ on the basis of the new posterior (see Step 3) to find the optimal $\boldsymbol{\theta}$. A detailed explanation of each step can be seen in Snoek et al., (2012). It is worth noting that the BO algorithm is only applied to find the optimal hyperparameter (i.e., number of hidden layers in the ANN model) and must not be used in the training process of the ML models (i.e., to optimize the weights of the ANN model). These two processes are completely different. Hereafter, the results and discussion are introduced.

Results and discussion

Experimental results

Track surface morphology

In this study, the surface morphologies of single tracks printed by SLM can be classified into three categories, depending on laser power and scanning speed, as shown in Fig. 4: continuous and homogenous track (Fig. 4a, b), continuous and non-homogeneous track (Fig. 4c), and irregular track (Fig. 4d). The single track deposited with high energy density, i.e., high laser power and low scanning speed, tends to form continuous tracks with homogenous width along the track except for the two extremities with rounded and wider shapes, as can be seen from Fig. 4. This may be due to the speed ramping of the laser beam at the start and the end of a deposition, especially a laser scanning speed fluctuation when moving from a track to another one. As the energy density is diminished, the track width decreases progressively. When the energy density continues to decrease, for example, keeping the laser power and increasing the scanning speed (see Fig. 5), the energy input becomes insufficient
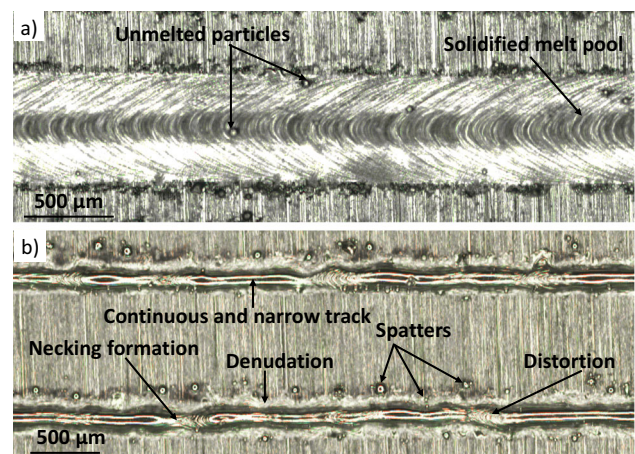
to homogeneously melt the metal particles, single tracks are noticed more and more unstable and inconstant, the necking formation is observed between short and narrow tracks, as shown in Fig. 6b. The last track type observed in this study consists of semi-continuous tracks with the presence of a nearly-spherical shape. This phenomenon is commonly observed when the energy input is too low to melt the metal powder, leading to a high viscosity of the molten pool and poor wettability (Di et al., 2012).

In this study, a severe balling effect is not observed. This may be explained by a relatively thin layer thickness, which may help to improve the bounding between deposited tracks and the substrate and reduce the formation of balling effect (Di et al., 2012; Yadroitsev & Smurov, 2010). The irregular surface morphology observed in Fig. 4.d may result from the humping effect (Gunenthiram et al., 2018) noticed at very high laser power and scanning speed. The balling and humping effects are sometimes confusing due to their nearly similar surface morphologies. However, the difference between these two phenomena lies in the depth penetration

of the tracks into the substrate or the previously printed layers. More precisely, the balling effect is caused by the lack of dilution due to low energy density, while the humping effect is observed with a combination of high laser power and scanning speed, consisting of a variation of melt pool along the track. The latter mainly results from a large length-to-width track ratio, which can promote the Rayleigh-Plateau instability (Gunenthiram et al., 2018). These phenomena will be discussed more in detail in the next part with the bead characteristics.

Figure 6 shows typical surface defects observed in SLM. At high energy, the spatters, consisting of unmelted particles, can be noticed trapped into the tracks (see Fig. 6a) or along the tracks (see Fig. 6b). They are also found at the end and in front of the track, as shown in Fig. 4a. These spatters can be considered as defects that strongly affect the laser stability and the mechanical properties of the final items fabricated by the SLM process. The origin of the spatters has been mainly assumed to be a result of the melt pool instability caused by the recoil pressure during the process (Khairallah et al., 2016). The amount and size of the spatters can be considerably reduced by increasing the laser power or lowering the scanning speed as reported in Gunenthiram et al., (2018), Taheri Andani et al., (2018). Along with this phenomenon, single tracks deposited by very high energy density are found to be covered by a thin black layer on their surface, as seen in Fig. 4a. This may be due to (1) the surface oxidation and (2) the vapor flow plume resulting from metal vaporization, which may pollute the track surface. Besides, Gunenthiram et al. reported that the higher the energy density, the closer to the track surface the vapor flow plume (Gunenthiram et al., 2018). Finally, the denudation consisting of a presence of powder-depleted areas near printed tracks is also observed in our study. Matthews et al. proposed that the denudation areas are created by blowing away the power around the melt pool during single track deposition (Matthews et al., 2016). This phenomenon may be due to the interaction recoil pressure—melt pool—powder particles or argon protection gas—powder particles, depending on the SLM chamber's environmental gas pressure (Matthews et al., 2016). The denudation cannot be considered as a defect, but it should be carefully taken into account when choosing the hatch distance between successive tracks to avoid the lack of fusion. However, it should be noted that profound insights about the formation and propagation of the defects during the process, as well as their impact on ultimate mechanical properties, are needed to be thoroughly investigated at different scales, macroscopic and microscopic. Besides, it is worthy performing the characterizations not only on single tracks, but also on thin walls, then bulk components fabricated by the SLM process. This could be the subject of our ongoing studies.
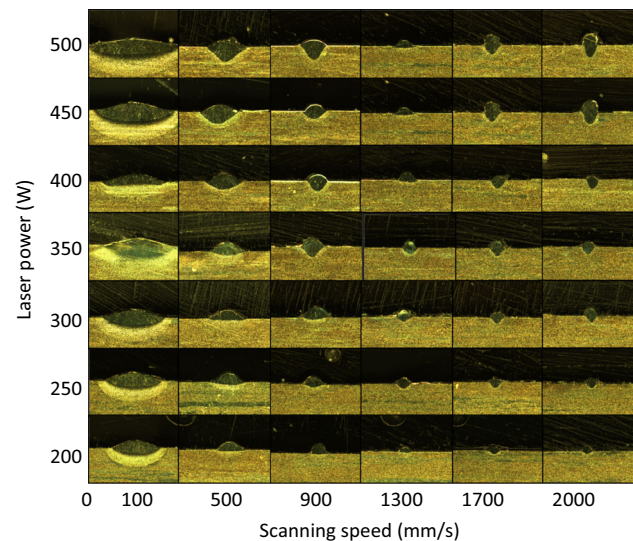

Fig. 7 Examples of SLM-printed bead profiles as a function of laser power and scanning speed

Measured bead geometric characteristics

The previous section discussed the main surface morphologies of 840 single tracks performed in our study. In this section, the effects of laser power and scanning speed on the bead characteristics, including bead depth, height, and width, as well as two aspect ratios (depth-to-width and height-to-width ratios), will be detailed.

Figure 7 summarizes the main bead profiles obtained in this study for different laser powers and scanning speeds. It can be seen that the cross-sectional morphologies of the melt pool are all dense with elliptical or nearly-spherical shapes. Besides, the keyhole effect, characterized by a very large penetration depth and usually the presence of pores caused by gas and alloy element evaporation entrapped in the bead, as shown in King et al., (2014), is not noticed for all combinations of laser power and scanning speed used. This phenomenon is commonly accepted as a result of excessively high energy (King et al., 2014).

Figures 8 and 9 show the influence of laser power and scanning speed on the bead depth, width, and height, respectively. The bead dimensions in occasionally discontinuous zones of the single tracks were not taken into account. The error bars represent the standard deviation from 6 repeated experiments for each laser power and scanning speed combination, as mentioned earlier. When the laser power or scanning speed is extremely high, the standard deviation becomes more significant. This is mainly due to the uncertainty and variation in the bead height and penetration depth measurements in such conditions.

As shown in Fig. 8, it can be seen that the bead depth and width increase continuously and in a roughly linear trend
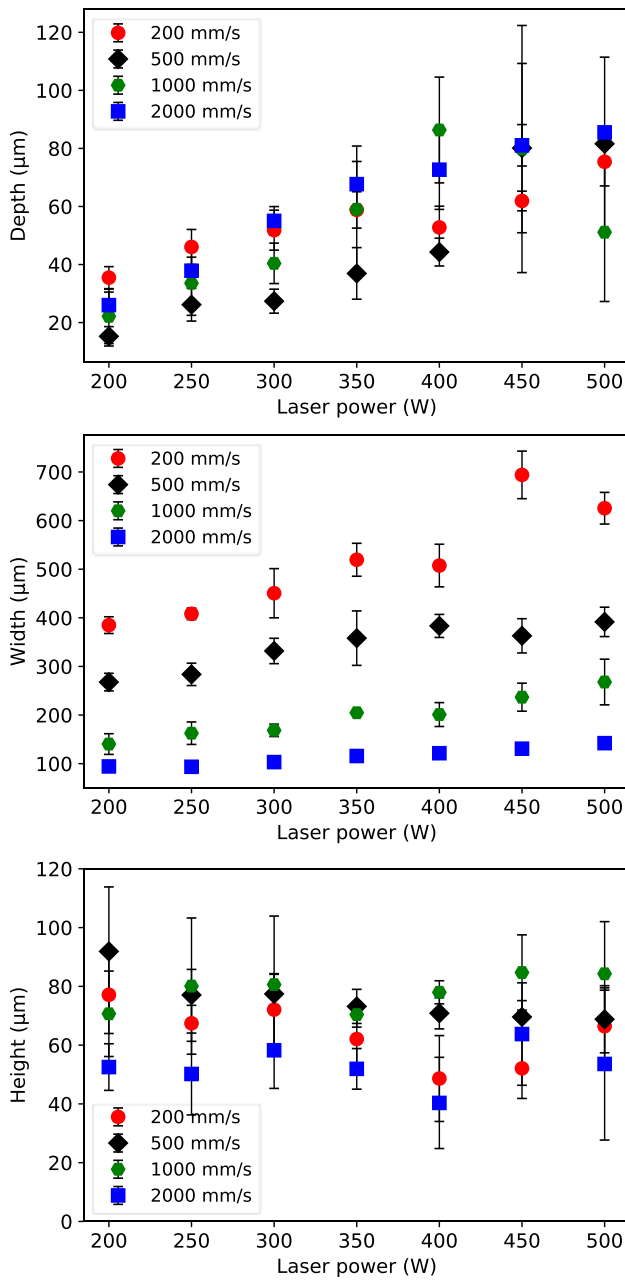
Fig. 8 Laser power dependence of the bead depth, width, and height for different scanning speeds (200, 500, 1000, and 2000 mm/s)

Fig. 9 Scanning speed dependence of the bead depth, width, and height for different laser power levels (200, 350, and 500 W)

as the laser power increases. This can be explained by an increased energy input absorbed by the metal powders, which tends to deepen and widen the created melt pool. Regarding the bead height, which varies between about 40 and 90 μm, it appears that it decreases slightly with the laser power, especially for low and moderate scanning speed, which may be due to a diminution in the viscosity of the molten pool, leading to an improved wetting ability. However, at high scanning speed, the bead height's evolution appears to be more complex, which may result from the instability of the molten
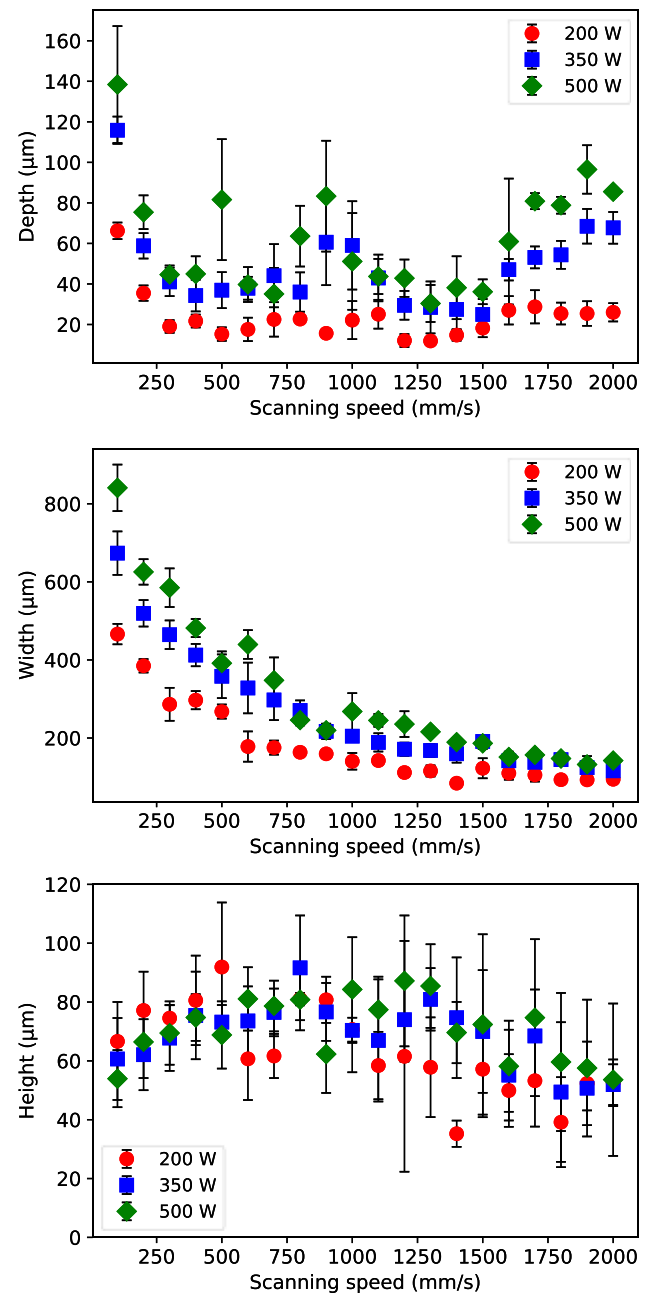
pool and humping effect at high scanning speed and high laser power, as discussed previously. This result is consistent with the observation reported in Li et al., (2017) and Scipioni Bertoli et al., (2017).

As shown in Fig. 9 for the scanning speed, a significant effect is noticed for the scanning speed between 100 mm/s and about 500 mm/s on the penetration depth, then it becomes less noticeable for higher scanning speed, especially at low laser power. The smallest depth measured in this study is about 10–15 μm for a laser power of 200 W and scan-

ning speeds varying from 500 to 1500 mm/s. In these conditions, the penetration depth seems to be small with a nearly-spherical bead shape and nearly right contact angle, as shown in Fig. 7. Besides, the surface track observations show that the tracks deposited with this laser power and scanning speed remain semi-continuous, assuring that no severe balling effect can occur (see Fig. 5). At high laser power, i.e., from 350 W, the penetration depth appears to increase with the scanning speed varying between 1500 and 2000 mm/s. This trend may be attributed to the humping effect occurring at very high laser power and scanning speed, as discussed in Gunenthiram et al., (2018).

The bead width tends to decrease considerably as the scanning speed increases due to a decrease in the energy density to melt the metal particle. As for the bead height, it seems that it increases with the scanning speed up to 1000–1200 mm/s, then decreases for the higher scanning speed. This appears to be in good agreement with the results observed by Li et al. (2017) for Inconel 625 and scanning speeds of 500–2500 mm/s. In contrast to the laser power's effect, at low scanning speed, the energy input tends to be diminished as the scanning speed increases, leading to an increase of the molten pool's viscosity and wetting ability. However, very high scanning speeds cause unstable/insufficient energy, leading to several phenomena in the molten pool, such as humping, denudation, etc., as discussed in Sect. 4.1.2, which may result in the bead height fluctuation of the printed tracks.

The effects of laser power and scanning speed on the evolution of two aspect ratios, D/W and H/W, are presented in Figs. 10 and 11. It can be seen that the maximum values of D/W and H/W ratios obtained in this study are about 0.8 and 0.6, respectively, with the smallest values of about 0.1. This can help to reconfirm the absence of both balling and keyhole mode.

Regarding the evolution of these two ratios, on the whole, the D/W ratio tends to increase gradually while the H/W ratio decreases progressively with increasing the laser power, as shown in Fig. 10. Besides, it seems that the laser power-related effect is intensified as the scanning speed increases from 200 to 2000 mm/s. More precisely, for 200 mm/s of scanning speed, the D/W ratio appears to remain constant as the laser power increases from 200 to 500 W. However, it should be noted that for the laser power higher than 400 W, the D/W ratio decreases slightly with the laser power for high scanning speed, for example, between 1500 and 2000 mm/s. This is probably due to the variation of the penetration depth, as mentioned earlier in this section. In summary, the relationship between the D/W ratio and the laser power seems not to be monotone. Nevertheless, a nearly-linear relationship can be noticed between the H/W ratio and the laser power, as illustrated in Fig. 10. However, at very high laser power and scanning speed,

the relationship becomes slightly different with fluctuation.

In contrast to the laser power, the effect of the scanning speed appears to be more complex, as shown in Fig. 11. Indeed, the evolution of the D/W ratio with the scanning speed is found to be similar to that observed on the penetration depth, as shown in Fig. 9. More precisely, it exhibits a diminution for scanning speeds from 100 to 500 mm/s followed by a nearly-steady trend for scanning speed between 500 and 1500 mm/s; then, it increases considerably for higher scanning speeds. Nonetheless, the bead width decreases continuously with the increase in the scanning speed, as shown in Fig. 9. Although the scanning speed seems not to exhibit a clear effect on the height, the H/W is noticed to increase continuously as the scanning speed increases. However, some fluctuations can be observed, especially for high scanning speed and high laser power.

Fitting curve-based prediction of bead characteristics

In the previous sections, the bead characteristics were deeply investigated with different laser powers and scanning speeds. This section aims to provide models that can help predict the two aspect ratios with regard to laser power and scanning speed. These models can be used for optimization frameworks that facilitate the SLM processing parameter selection to obtain suitable bead characteristics.

In this study, several simple models based on linear, polynomial, and exponential relationships were developed, as the first approach, to describe the evolutions of the D/W and H/W ratios as a function of two process parameters, i.e., laser power and scanning speed. Table 3 lists the models based on simple mathematical equations used in this study. These equations were chosen purely by observing the evolutions of the two aspect ratios, D/W and H/W, measured experimentally as a function of the laser power and scanning speed (see Figs. 10 and 11). Besides, Model 2 was tested, following the example of the study reported in Shi et al., (2017). It should be noted that none of the two aspect ratios measured in our study can exhibit a significant relationship with the laser power-to-scanning speed ratio (P/v).

Table 4 presents the R^2 values obtained using the simple models for the prediction of the two aspect ratios, D/W and H/W. It can be seen that the accuracy of these models remains very limited, with relatively low R^2 values, due to complex evolutions of these ratios and their quality that is highly affected by noise due to uncertainty resulting from experimental conditions or/and measurement methods, as mentioned previously. Additionally, Model 2
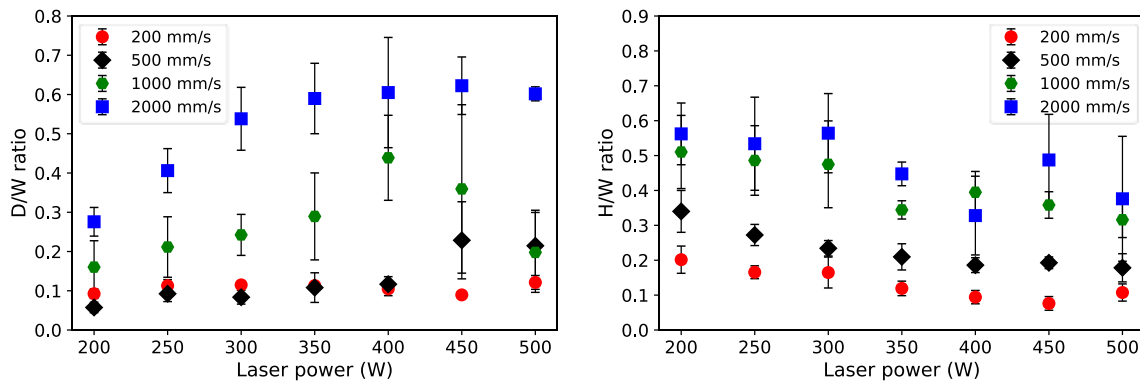
Fig. 10 Laser power dependence of the D/W and H/W ratios for different scanning speeds (200, 500, 1000, and 2000 mm/s)
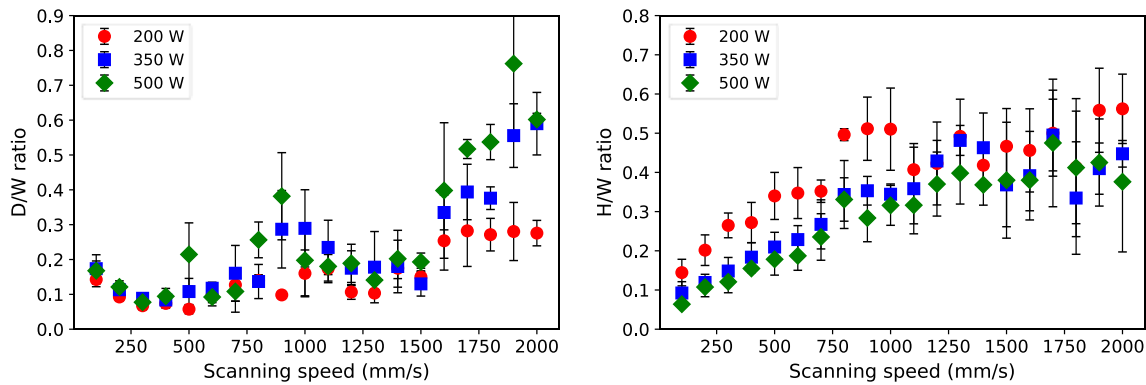

Fig. 11 Scanning speed dependence of the D/W and H/W ratios for different laser power levels (200, 350, and 500 W)

Table 3 Summary of the simple fitting curve-based models used for the aspect ratio predictions

Model	Equation
Model 1	$y = a(1 + bP)(1 + cv)$
Model 2	$y = aP^b v^c$
Model 3	$y = a(1 + bP)(1 + cv + dv^2)$
Model 4	$y = a(1 + bP + cP^2)(1 + dv)$
Model 5	$y = a(1 + bP + cP^2)(1 + dv + ev^2)$

Table 4 R^2 values obtained by the simple models listed in Table 3 for two aspect ratios, D/W and H/W

	Model 1	Model 2	Model 3	Model 4	Model 5
D/W ratio	0.47	0.44	0.69	0.55	0.70
H/W ratio	0.68	–	0.75	0.70	0.78

is not suitable for the H/W prediction, expressed by a negative value of R^2. Besides, it should be emphasized that the fitting curves were established, and their corresponding R^2 values were calculated through the whole dataset, leading to potentially higher R^2 values. As a result, Machine Learning-based models were employed in the hope of improving the model accuracy, as discussed hereafter in this section. It has been shown that the ML-based methods become helpful for dealing with complex situations with multidimensional datasets composed of a huge data number and without requiring existing physics-based equations.

Machine learning-based prediction of bead characteristics

Model hyperparameter selection

In our study, the Bayesian optimization for hyperparameter tuning was performed using the gp_optimize package provided by the Scikit-Optimize library (Skopt) in Python version 3.7.3. The TensorFlow and Keras libraries were used for the artificial neural network. First, the algorithm is applied to the dataset using the initial set of hyperparameters defined by the user, known as default parameters, to compute the corresponding loss value in the validation dataset. The next sets of hyperparameters will be identified in each iteration, called *n_call*, by the Bayesian optimization algorithm, from their predefined ranges to minimize the target function, i.e., Mean Squared Error (MSE) for ANN and the negative value

of the R^2 for Random Forest model. The MSE is calculated as follows:

$$MSE = \frac{1}{n} \sum_{i=1}^{n} (y_i - \widehat{y_i})^2 \tag{7}$$

where y_i, $\widehat{y_i}$, and n are the actual value, the predicted value from the model, and the number of samples in the dataset, respectively. It should be noted that the dataset was beforehand split into training and validation datasets, as mentioned previously. The training set is used to train the model for this task; then, the hyperparameter optimization process is performed on the validation set. In this study, Bayesian optimization was employed to search for the best sets of model architecture (number of hidden layers, number of neurons in each hidden layer), dropout rate, learning rate for the ANN model. Regarding the Random Forest model, 4 hyperparameters, namely max depth, min samples leaf, min samples split, and the number of estimators, were tuned using the Bayesian optimization. As mentioned in Sect. 3.2, Random Forest is an ML-based algorithm widely used for regression and classification, which is based on the learning of multiple decision trees that are randomly constructed from the sub-samples of the whole dataset. 4 hyperparameters, which are tuned using the BO algorithm, correspond to the maximum depth of the tree, the minimum number of samples required at a leaf node, the minimum number of samples required for an internal node, and the number of trees.

Figure 12 shows the lowest mean squared error optimized for each iteration by the Bayesian optimization algorithm for the ANN hyperparameters. The optimization process can converge rapidly after about 20 iterations to obtain an MSE lower than only 0.007. Besides, in the beginning, the MSE obtained seems to be constant with a relatively low value. This may be explained by the fact that the initial set of hyperparameters selected is quite good, leading to reasonably good results. In terms of tuning time, the algorithm took about 46 min to tune 5 hyperparameters of the ANN models with 40 iterations, 4000 epochs for each iteration, as against about 33 min for 4 Random Forest model parameters with 400 iterations.

Tables 5 and 6 list the parameters used in this study for the ANN and Random Forest models. In general, the larger the max depth value; in other words, the deeper the decision trees are allowed to grow, the more complex the model becomes and the more it can capture information from data. However, this may cause overfitting in the case of an excessively complex model. The max features correspond to the number of features that the model considers when looking for the best split. In our model, the 'auto' option was chosen to speed up the tree's stability and training process. The number of estimators consists of the number of samples on which the algorithm will work, then averages the predictive result.
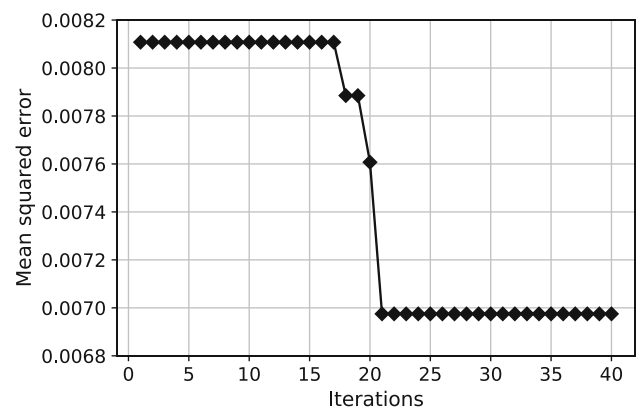

Fig. 12 Convergence trace obtained by the Bayesian optimization algorithm for ANN hyperparameter tuning
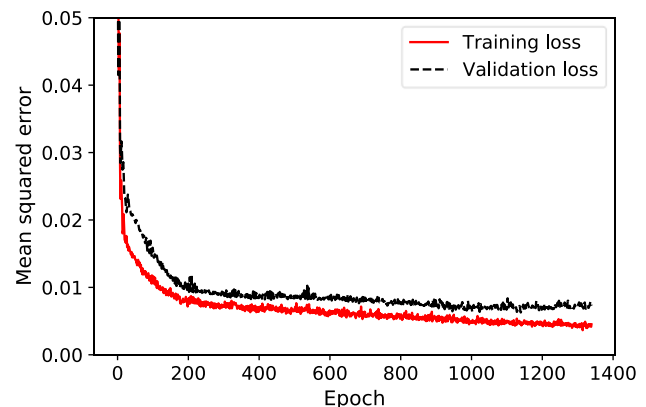

Fig. 13 Training and validation losses of the ANN model as a function of epoch

The higher the number of trees, the better performance the model can achieve, but this can considerably slow down the calculation.

Note that in the ANN model, there are 4 layers in which the first and last layers with 2 nodes for each layer correspond to the number of input and output variables. Additionally, the model contains 2 hidden layers constituted of 503 and 19 nodes, respectively. Besides, dropout regularization and EarlyStopping were used to deal with the overfitting issue that may occur in the case of complex ANN model architecture (Dahl et al., 2013; Goodfellow et al., 2016). Other hyperparameters, including Adam optimizer (Kingma & Ba, 2017) and ReLU activation function (Nair & Hinton, 2010), were used in the optimization algorithm to minimize the MSE loss function of the neural network for the predictive model presented in Sect. 4.3.2 for the prediction of bead characteristics.

Table 5 ANN model hyperparameters

Model architecture	Loss function	Activation function	Optimizer	Dropout rate	Learning rate
2–503–19–2	MSE	ReLU	Adam	0.1	0.007

Table 6 Random Forest model parameters

Max depth	Max features	Min samples leaf	Min samples split	Number of estimators
110	'auto'	1	2	100

Table 7 Summary results obtained by the ANN and Random Forest models for D/W and H/W ratios

	Training				Validation		
	Overall R^2 (%)	D/W R^2 (%)	H/W R^2 (%)	Training time (s)	Overall R^2 (%)	D/W R^2 (%)	H/W R^2 (%)
ANN	95.8	98.7	92.9	18.27	90.4	92.4	88.4
Random forest	98.0	98.1	97.9	0.05	85.6	90.4	80.8

Machine learning-based model performance

Figure 13 shows the evolution of the loss function (mean squared error) in each epoch for the training and validation processes of the ANN model. Note that an epoch consists of an entire process of training and validation. It can be seen that the model converges relatively rapidly, after only about 18 s (see Table 7), to reach a satisfactorily low value of losses for both training and validation processes. Besides, neither overfitting nor underfitting is observed for our model. This can help to assure the reliability of the results obtained. In terms of the training time, it is shown in Table 7 that the Random Forest needs much less time to finish the whole process, only 0.05 s as against 18 s in the case of the ANN model.

Regarding the model performance, Fig. 14 indicates that both ANN and Random Forest models are capable of estimating reasonably well the two aspect ratios, D/W and H/W, using two process parameters, with satisfactorily good accuracy of 85–90% of R^2 assessed on the validation dataset that is never seen before by the model. However, it seems that the models tend to underfit the two ratios at very high values. Nevertheless, it can be seen from Fig. 14 that the models can predict very well both D/W and H/W ratios with values smaller than 0.6. It should be noted that these value ranges are expected to provide good printed bead quality, as mentioned earlier in the introduction. In other words, the model accuracy could be significantly increased by considering only the D/W and H/W ratios' values below 0.6. Besides, as shown in Table 7, the models can estimate the D/W ratio more accurately than the H/W ratio, although the latter's relationships with the laser power and scanning speed seem to be less complex, as discussed in Sect. 4.1.2. The results presented in this section indicate that ML-based models are useful to develop a prediction tool.

Conclusion

In order to obtain high-quality items fabricated by the SLM process with fewer defects, it is vital to thoroughly investigate the effects of two key process parameters, namely laser power and scanning speed, on the single-track characteristics. In this study, 840 single tracks were printed by the SLM process with various laser power and scanning speed levels, covering a large range of values, from very low to very high. The bead geometric characteristics, i.e., depth, width, height, as well as two aspect ratios, penetration depth-to-bead width D/W and bead height-to-width H/W ratios, were characterized using both experimental and Machine Learning approaches.

From the experimental point of view, among the important findings:

- Several surface morphologies of the single tracks and bead profiles were thoroughly investigated, providing a track-type map and the evolutions of the bead characteristics as a function of laser power and scanning speed.
- The observations performed on the track surface, as well as the analyses of the bead characteristics at the cross-section, indicate neither severe balling nor keyhole mode for all the combinations of laser power and scanning speed adopted in this study.
- Three types of single tracks are noticed: continuous and homogeneous track, continuous and non-homogeneous track, and irregular track, depending on laser power and scanning speed.
- The bead characteristics' evolutions are found not to be monotone and strongly depend on the laser power and scanning speed levels.
- This helps provide a complete experimental database for the bead characteristics as a function of process parame-
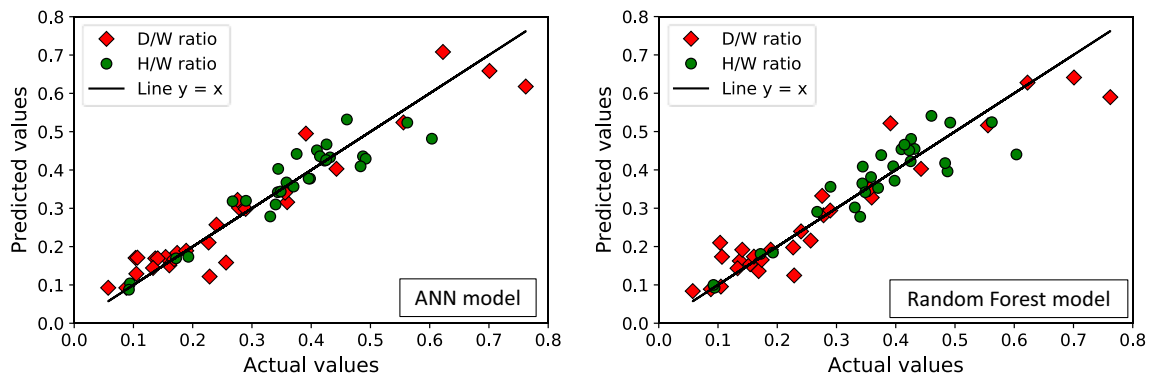
Fig. 14 Comparison of the D/W and H/W ratios' values in the validation dataset with those predicted by the ANN and Random Forest models

ters, as well as an in-depth understanding of the complex relationship between them.

In order to predict the bead geometry using laser power and scanning speed, several fitting curves based on simple relationships were proposed as the first approach. It is shown that they are unable to sufficiently accurately predict the evolutions of the D/W and H/W ratios as a function of laser power and scanning speed, with relatively low R^2 values, due to the complexity in the evolutions of these ratios.

Regarding the application of Machine Learning:

- Two Machine Learning-based regression models, including Random Forest and Artificial Neural Network, were employed to estimate the D/W and H/W ratios using laser power and scanning speed. Besides, the Bayesian optimization algorithm was employed to optimize the model hyperparameter selection in an automated way with more accuracy.
- The results obtained by the numerical approach show that both models are capable of predicting reasonably well the two aspect ratios, D/W and H/W, with an overall accuracy up to 90% of R^2 evaluated on an unseen dataset and an R^2 reaching 98–99% for the training dataset, after only a few seconds to about tenths of seconds of training time.
- The results indicate that Machine Learning is useful to develop a prediction tool for additive manufacturing field-relevant applications.

These models are expected to be used to develop optimization frameworks based on Machine Learning methods, which can help facilitate the process parameter selection to obtain target characteristics of single-track and multi-track depositions and bulk components fabricated by the SLM process. This is also the next step of our work in the future.

Supplementary Information The online version contains supplementary material available at https://doi.org/10.1007/s10845-021-01845-5.

References

Ahsan, F., & Ladani, L. (2020). Temperature profile, bead geometry, and elemental evaporation in laser powder bed fusion additive manufacturing process. *JOM Journal of the Minerals Metals and Materials Society, 72*(1), 429–439. https://doi.org/10.1007/s11837-019-03872-3

Aldous, D. (1993). The continuum random tree III. *The Annals of Probability, 21*(1), 248–289. https://doi.org/10.1214/aop/1176989404

Andreotta, R., Ladani, L., & Brindley, W. (2017). Finite element simulation of laser additive melting and solidification of Inconel 718 with experimentally tested thermal properties. *Finite Elements in Analysis and Design, 135*, 36–43. https://doi.org/10.1016/j.finel.2017.07.002

Dahl, G. E., Sainath, T. N., & Hinton, G. E. (2013). Improving deep neural networks for LVCSR using rectified linear units and dropout (pp. 8609–8613). Presented at the 2013 IEEE International Conference on Acoustics, Speech and Signal Processing. https://doi.org/10.1109/ICASSP.2013.6639346

Di, W., Yongqiang, Y., Xubin, S., & Yonghua, C. (2012). Study on energy input and its influences on single-track, multi-track, and multi-layer in SLM. *The International Journal of Advanced Manufacturing Technology, 58*(9), 1189–1199. https://doi.org/10.1007/s00170-011-3443-y

Dilip, J. J. S., Zhang, S., Teng, C., Zeng, K., Robinson, C., Pal, D., & Stucker, B. (2017). Influence of processing parameters on the evolution of melt pool, porosity, and microstructures in Ti–6Al–4V alloy parts fabricated by selective laser melting. *Progress in Additive Manufacturing, 2*(3), 157–167. https://doi.org/10.1007/s40964-017-0030-2

Dutta, B., & Froes, F. H. (2017). The additive manufacturing (AM) of titanium alloys. *Metal Powder Report, 72*(2), 96–106. https://doi.org/10.1016/j.mprp.2016.12.062

Frazier, P. I. (2018). A tutorial on Bayesian optimization. arXiv:1807.02811 [cs, math, stat]. Accessed 11 May 2021.

Gao, J., Wu, C., Hao, Y., Xu, X., & Guo, L. (2020). Numerical simulation and experimental investigation on three-dimensional modelling of single-track geometry and temperature evolution by laser cladding. *Optics & Laser Technology, 129*, 106287. https://doi.org/10.1016/j.optlastec.2020.106287

Garg, A., Lam, J. S. L., & Savalani, M. M. (2018). Laser power based surface characteristics models for 3-D printing process. *Journal of*

Intelligent Manufacturing, 29(6), 1191–1202. https://doi.org/10.1007/s10845-015-1167-9

Goodfellow, I., Bengio, Y., & Courville, A. (2016). *Deep learning*. The MIT Press.

Greco, S., Gutzeit, K., Hotz, H., Kirsch, B., & Aurich, J. C. (2020). Selective laser melting (SLM) of AISI 316L—Impact of laser power, layer thickness, and hatch spacing on roughness, density, and microhardness at constant input energy density. *The International Journal of Advanced Manufacturing Technology, 108*(5), 1551–1562. https://doi.org/10.1007/s00170-020-05510-8

Gu, H., Wei, C., Li, L., Han, Q., Setchi, R., Ryan, M., & Li, Q. (2020). Multi-physics modelling of molten pool development and track formation in multi-track, multi-layer and multi-material selective laser melting. *International Journal of Heat and Mass Transfer, 151*, 119458. https://doi.org/10.1016/j.ijheatmasstransfer.2020.119458

Gunenthiram, V., Peyre, P., Schneider, M., Dal, M., Coste, F., Koutiri, I., & Fabbro, R. (2018). Experimental analysis of spatter generation and melt-pool behavior during the powder bed laser beam melting process. *Journal of Materials Processing Technology, 251*, 376–386. https://doi.org/10.1016/j.jmatprotec.2017.08.012

Guo, M., Gu, D., Xi, L., Du, L., Zhang, H., & Zhang, J. (2019). Formation of scanning tracks during Selective Laser Melting (SLM) of pure tungsten powder: Morphology, geometric features and forming mechanisms. *International Journal of Refractory Metals and Hard Materials, 79*, 37–46. https://doi.org/10.1016/j.ijrmhm.2018.11.003

He, Y., Montgomery, C., Beuth, J., & Webler, B. (2019). Melt pool geometry and microstructure of Ti6Al4V with B additions processed by selective laser melting additive manufacturing. *Materials & Design, 183*, 108126. https://doi.org/10.1016/j.matdes.2019.108126

Heumann, C., & Schomaker, M. (2016). *Introduction to statistics and data analysis: With exercises, solutions and applications in R*. Springer. https://doi.org/10.1007/978-3-319-46162-5

Jain, A. K., Mao, J., & Mohiuddin, K. M. (1996). Artificial neural networks: A tutorial. *Computer, 29*(3), 31–44. https://doi.org/10.1109/2.485891

Kamath, C. (2016). Data mining and statistical inference in selective laser melting. *The International Journal of Advanced Manufacturing Technology, 86*(5), 1659–1677. https://doi.org/10.1007/s00170-015-8289-2

Khairallah, S. A., Anderson, A. T., Rubenchik, A., & King, W. E. (2016). Laser powder-bed fusion additive manufacturing: Physics of complex melt flow and formation mechanisms of pores, spatter, and denudation zones. *Acta Materialia, 108*, 36–45. https://doi.org/10.1016/j.actamat.2016.02.014

Khanzadeh, M., Chowdhury, S., Marufuzzaman, M., Tschopp, M. A., & Bian, L. (2018). Porosity prediction: Supervised-learning of thermal history for direct laser deposition. *Journal of Manufacturing Systems, 47*, 69–82. https://doi.org/10.1016/j.jmsy.2018.04.001

Khanzadeh, M., Chowdhury, S., Tschopp, M. A., Doude, H. R., Marufuzzaman, M., & Bian, L. (2019). In-situ monitoring of melt pool images for porosity prediction in directed energy deposition processes. *IISE Transactions, 51*(5), 437–455. https://doi.org/10.1080/24725854.2017.1417656

King, W. E., Barth, H. D., Castillo, V. M., Gallegos, G. F., Gibbs, J. W., Hahn, D. E., et al. (2014). Observation of keyhole-mode laser melting in laser powder-bed fusion additive manufacturing. *Journal of Materials Processing Technology, 214*(12), 2915–2925. https://doi.org/10.1016/j.jmatprotec.2014.06.005

Kingma, D. P., & Ba, J. (2017). Adam: A method for stochastic optimization. arXiv:1412.6980 [cs]. Accessed 11 May 2021.

Kistler, N. A., Corbin, D. J., Nassar, A. R., Reutzel, E. W., & Beese, A. M. (2019). Effect of processing conditions on the microstructure, porosity, and mechanical properties of Ti–6Al–4V repair fabricated by directed energy deposition. *Journal of Materials Processing Technology, 264*, 172–181. https://doi.org/10.1016/j.jmatprotec.2018.08.041

Kusuma, C., Ahmed, S. H., Mian, A., & Srinivasan, R. (2017). Effect of laser power and scan speed on melt pool characteristics of commercially pure titanium (CP-Ti). *Journal of Materials Engineering and Performance, 26*(7), 3560–3568. https://doi.org/10.1007/s11665-017-2768-6

Le, T.-N., & Lo, Y.-L. (2019). Effects of sulfur concentration and Marangoni convection on melt-pool formation in transition mode of selective laser melting process. *Materials & Design, 179*, 107866. https://doi.org/10.1016/j.matdes.2019.107866

Le, T.-N., Lo, Y.-L., & Lin, Z.-H. (2020). Numerical simulation and experimental validation of melting and solidification process in selective laser melting of IN718 alloy. *Additive Manufacturing, 36*, 101519. https://doi.org/10.1016/j.addma.2020.101519

Leal, R., Barreiros, F. M., Alves, L., Romeiro, F., Vasco, J. C., Santos, M., & Marto, C. (2017). Additive manufacturing tooling for the automotive industry. *The International Journal of Advanced Manufacturing Technology, 92*(5), 1671–1676. https://doi.org/10.1007/s00170-017-0239-8

Li, C., Guo, Y. B., & Zhao, J. B. (2017). Interfacial phenomena and characteristics between the deposited material and substrate in selective laser melting Inconel 625. *Journal of Materials Processing Technology, 243*, 269–281. https://doi.org/10.1016/j.jmatprotec.2016.12.033

Mahamood, R. M., & Akinlabi, E. T. (2018). Heat affected zone relationship with processing parameter in additive manufacturing process. *Materials Today: Proceedings, 5*(9, Part 3), 18362–18367. https://doi.org/10.1016/j.matpr.2018.06.175

Matthews, M. J., Guss, G., Khairallah, S. A., Rubenchik, A. M., Depond, P. J., & King, W. E. (2016). Denudation of metal powder layers in laser powder bed fusion processes. *Acta Materialia, 114*, 33–42. https://doi.org/10.1016/j.actamat.2016.05.017

Meng, L., McWilliams, B., Jarosinski, W., Park, H.-Y., Jung, Y.-G., Lee, J., & Zhang, J. (2020). Machine learning in additive manufacturing: A review. *JOM Journal of the Minerals Metals and Materials Society, 72*(6), 2363–2377. https://doi.org/10.1007/s11837-020-04155-y

Mohajernia, B., Urbanic, R. J., & Nazemi, N. (2019). Predictive modelling of residual stresses for single bead P420 laser cladding onto an AISI 1018 substrate. *IFAC-PapersOnLine, 52*(10), 236–241. https://doi.org/10.1016/j.ifacol.2019.10.070

Mohd Yusuf, S., Cutler, S., & Gao, N. (2019). Review: The impact of metal additive manufacturing on the aerospace industry. *Metals, 9*(12), 1286. https://doi.org/10.3390/met9121286

Mozaffar, M., Paul, A., Al-Bahrani, R., Wolff, S., Choudhary, A., Agrawal, A., et al. (2018). Data-driven prediction of the high-dimensional thermal history in directed energy deposition processes via recurrent neural networks. *Manufacturing Letters, 18*, 35–39. https://doi.org/10.1016/j.mfglet.2018.10.002

Nair, V., & Hinton, G. E. (2010). Rectified linear units improve restricted boltzmann machines. In *Proceedings of the 27th international conference on international conference on machine learning* (pp. 807–814). Madison, WI, USA: Omnipress. Accessed 11 May 2021.

Panda, B., Shankhwar, K., Garg, A., & Savalani, M. M. (2019). Evaluation of genetic programming-based models for simulating bead dimensions in wire and arc additive manufacturing. *Journal of Intelligent Manufacturing, 30*(2), 809–820. https://doi.org/10.1007/s10845-016-1282-2

Papazoglou, E. L., Karkalos, N. E., & Markopoulos, A. P. (2020). A comprehensive study on thermal modeling of SLM process under conduction mode using FEM. *The International Journal of Advanced Manufacturing Technology, 111*(9), 2939–2955. https://doi.org/10.1007/s00170-020-06294-7

Park, H. S., Nguyen, D. S., Le-Hong, T., & Van Tran, X. (2021). Machine learning-based optimization of process parameters in selective laser melting for biomedical applications. *Journal of Intelligent Manufacturing*. https://doi.org/10.1007/s10845-021-01773-4

Qi, T., Zhu, H., Zhang, H., Yin, J., Ke, L., & Zeng, X. (2017). Selective laser melting of Al7050 powder: Melting mode transition and comparison of the characteristics between the keyhole and conduction mode. *Materials & Design, 135*, 257–266. https://doi.org/10.1016/j.matdes.2017.09.014

Qi, X., Chen, G., Li, Y., Cheng, X., & Li, C. (2019). Applying neural-network-based machine learning to additive manufacturing: Current applications, challenges, and future perspectives. *Engineering, 5*(4), 721–729. https://doi.org/10.1016/j.eng.2019.04.012

Ren, K., Chew, Y., Zhang, Y. F., Fuh, J. Y. H., & Bi, G. J. (2020). Thermal field prediction for laser scanning paths in laser aided additive manufacturing by physics-based machine learning. *Computer Methods in Applied Mechanics and Engineering, 362*, 112734. https://doi.org/10.1016/j.cma.2019.112734

Roy, M., & Wodo, O. (2020). Data-driven modeling of thermal history in additive manufacturing. *Additive Manufacturing, 32*, 101017. https://doi.org/10.1016/j.addma.2019.101017

Santos, E. C., Shiomi, M., Osakada, K., & Laoui, T. (2006). Rapid manufacturing of metal components by laser forming. *International Journal of Machine Tools and Manufacture, 46*(12), 1459–1468. https://doi.org/10.1016/j.ijmachtools.2005.09.005

Scime, L., & Beuth, J. (2019). Using machine learning to identify in-situ melt pool signatures indicative of flaw formation in a laser powder bed fusion additive manufacturing process. *Additive Manufacturing, 25*, 151–165. https://doi.org/10.1016/j.addma.2018.11.010

Scipioni Bertoli, U., Wolfer, A. J., Matthews, M. J., Delplanque, J.-P.R., & Schoenung, J. M. (2017). On the limitations of volumetric energy density as a design parameter for selective laser melting. *Materials & Design, 113*, 331–340. https://doi.org/10.1016/j.matdes.2016.10.037

Shi, X., Ma, S., Liu, C., & Wu, Q. (2017). Parameter optimization for Ti–47Al–2Cr–2Nb in selective laser melting based on geometric characteristics of single scan tracks. *Optics & Laser Technology, 90*, 71–79. https://doi.org/10.1016/j.optlastec.2016.11.002

Snoek, J., Larochelle, H., & Adams, R. P. (2012). Practical Bayesian optimization of machine learning algorithms. In *Proceedings of the 25th international conference on neural information processing systems—Volume 2* (pp. 2951–2959). Red Hook, NY, USA: Curran Associates Inc. Accessed 11 May 2021.

Taheri Andani, M., Dehghani, R., Karamooz-Ravari, M. R., Mirzaeifar, R., & Ni, J. (2018). A study on the effect of energy input on spatter particles creation during selective laser melting process. *Additive Manufacturing, 20*, 33–43. https://doi.org/10.1016/j.addma.2017.12.009

Tang, M., Pistorius, P. C., & Beuth, J. L. (2017). Prediction of lack-of-fusion porosity for powder bed fusion. *Additive Manufacturing, 14*, 39–48. https://doi.org/10.1016/j.addma.2016.12.001

Tapia, G., Khairallah, S., Matthews, M., King, W. E., & Elwany, A. (2018). Gaussian process-based surrogate modeling framework for process planning in laser powder-bed fusion additive manufacturing of 316L stainless steel. *The International Journal of Advanced Manufacturing Technology, 94*(9), 3591–3603. https://doi.org/10.1007/s00170-017-1045-z

Trevisan, F., Calignano, F., Aversa, A., Marchese, G., Lombardi, M., Biamino, S., et al. (2018). Additive manufacturing of titanium alloys in the biomedical field: Processes, properties and applications. *Journal of Applied Biomaterials & Functional Materials, 16*(2), 57–67. https://doi.org/10.5301/jabfm.5000371

Unpingco, J. (2019). *Python for probability, statistics, and machine learning* (2nd ed.). Springer. https://doi.org/10.1007/978-3-030-18545-9

Wang, C., Tan, X. P., Tor, S. B., & Lim, C. S. (2020a). Machine learning in additive manufacturing: State-of-the-art and perspectives. *Additive Manufacturing, 36*, 101538. https://doi.org/10.1016/j.addma.2020.101538

Wang, L., Silva, L., Süß-Wolf, R., & Franke, J. (2020b). Prediction of surface roughness of laser selective metallization of ceramics by multiple linear regression and artificial neural networks approaches. *Journal of Laser Applications, 32*(4), 042013. https://doi.org/10.2351/7.0000198

Xia, C., Pan, Z., Polden, J., Li, H., Xu, Y., & Chen, S. (2021). Modelling and prediction of surface roughness in wire arc additive manufacturing using machine learning. *Journal of Intelligent Manufacturing*. https://doi.org/10.1007/s10845-020-01725-4

Xiong, J., Zhang, G., Hu, J., & Wu, L. (2014). Bead geometry prediction for robotic GMAW-based rapid manufacturing through a neural network and a second-order regression analysis. *Journal of Intelligent Manufacturing, 25*(1), 157–163. https://doi.org/10.1007/s10845-012-0682-1

Yadroitsev, I., & Smurov, I. (2010). Selective laser melting technology: From the single laser melted track stability to 3D parts of complex shape. *Physics Procedia, 5*, 551–560. https://doi.org/10.1016/j.phpro.2010.08.083

Yang, J., Han, J., Yu, H., Yin, J., Gao, M., Wang, Z., & Zeng, X. (2016). Role of molten pool mode on formability, microstructure and mechanical properties of selective laser melted Ti–6Al–4V alloy. *Materials & Design, 110*, 558–570. https://doi.org/10.1016/j.matdes.2016.08.036

Yun, K., Huyen, A., & Lu, T. (2018). Deep neural networks for pattern recognition. In *Advances in pattern recognition research* (pp. 49–79).

Zhang, L., Zhang, S., Zhu, H., Hu, Z., Wang, G., & Zeng, X. (2018). Horizontal dimensional accuracy prediction of selective laser melting. *Materials & Design, 160*, 9–20. https://doi.org/10.1016/j.matdes.2018.08.059